Three-dimensional wave packets in a compressible boundary layer

Eric Forgoston and Anatoli Tumin
The University of Arizona, Tucson, Arizona 85721

(Received 13 February 2006; accepted 23 August 2006; published online 10 October 2006)

A three-dimensional wave packet generated by a local disturbance in a two-dimensional hypersonic boundary layer flow is studied with the aid of the previously solved initial-value problem. The solution to this problem can be expanded in a biorthogonal eigenfunction system as a sum of modes consisting of continuous and discrete spectra of temporal stability theory. A specific disturbance consisting of an initial temperature spot is considered, and the receptivity to this initial temperature spot is computed for both the two-dimensional and three-dimensional cases. Using previous analysis of the discrete and continuous spectrum, the inverse Fourier transform is computed numerically. The two-dimensional inverse Fourier transform is calculated for two discrete modes: Mode F and Mode S. The Mode S result is compared with an asymptotic approximation of the Fourier integral, which is obtained using the Gaussian model as well as the method of steepest descent. It is shown that the method of steepest descent provides an excellent approximation to the more computationally intensive numerical evaluation of the inverse Fourier transform. Additionally, the three-dimensional inverse Fourier transform is found using an asymptotic approximation of the Fourier integral. A main feature of the resulting three-dimensional wave packet is its two-dimensional nature, which arises from an association of Mode S with Mack's second mode. © *2006 American Institute of Physics*. [DOI: 10.1063/1.2359003]

I. INTRODUCTION

It is important to study the laminar-to-turbulent transition in hypersonic boundary layers due to the important role it will have in the development of future vehicles operating at hypersonic speeds. Aerodynamic heating on an aircraft changes dramatically when the laminar flow becomes turbulent. Since aerodynamic heating affects the choice of materials used for protecting the vehicle—and therefore the weight of the vehicle—the laminar-turbulent transition process must be understood.

The transition process from laminar to turbulent flow in hypersonic boundary layers has been studied for many years. However, because experimental conditions are so severe in hypersonic wind tunnels, our understanding of this phenomena is still very poor compared with the low speed case. Because of high levels of free-stream noise, it is difficult to perform experiments with controlled disturbances. Unlike the low speed case, it is difficult to design perturbers that can generate high-frequency artificial disturbances of individual modes. Instead, wave trains and wave packets are used in the experiment. Therefore, interpretation of experimental data is not straightforward, and this issue leads to the need for close coordination between theoretical modeling and experimental design and testing.

Several methods for excitation of artificial disturbances in a hypersonic boundary layer are available.[1–4] These methods could be used to generate either two-dimensional (2D) or three-dimensional (3D) wave packets of a broad frequency band. Additionally, due to advances in computational fluid dynamics, it is possible to perform reliable direct numerical simulations of laminar-turbulent transition to better understand the mechanisms leading to hypersonic boundary layer transition.[5–11]

Accompanying these experiments, both wind tunnel and numerical, should be theoretical modeling and studies of the development of wave packets in hypersonic boundary layers.

The dynamics of the flow transition depend on the instability of small perturbations excited by external sources. In investigating the stability of flows, the motion is decomposed into the basic flow whose stability is to be examined, and a superimposed perturbation. Linearization of the governing equations leads to a system of partial differential equations (PDEs). With a parallel flow approximation, Fourier and Laplace transforms can be used to transform these PDEs into a system of ordinary differential equations (ODEs). This set of ODEs, along with the associated boundary conditions, can be recast as an eigenvalue problem.

At this stage, the eigenmodes can be analyzed within the scope of a spatial theory or a temporal theory. For the spatial analysis, the frequency of the perturbation is prescribed to be real-valued, and one solves the eigenvalue problem for the complex-valued wave number. For the temporal analysis, one prescribes the wave number to be real-valued, and solves the eigenvalue problem for the complex-valued frequency. The signaling problem[12] is the physical problem associated with the spatial stability theory. The initial-value problem[13] is the physical problem associated with the temporal stability theory.

Gustavsson[13] solved a 2D initial-value problem for incompressible boundary layer flows. Fedorov and Tumin[14] analyzed a 2D initial-value problem in a compressible boundary layer with the use of Fourier and Laplace trans-

forms. However, they did not compute the inverse Fourier transform for the wave packet. Forgoston and Tumin[15] extended the work of Ref. 14 by solving the initial-value problem for 3D wave packets. Once again, the inverse Fourier transform was not computed.

Mack[16,17] used linear stability theory to perform extensive studies of the behavior of 2D and 3D instability modes for both the temporal and spatial problems. In particular, he discovered that for compressible flows, higher acoustic instability modes exist along with the first mode. However, even though the behavior of these modes is understood, the mechanism by which the modes are generated (receptivity problem) is still a subject of research. Throughout the 1980s, 1990s, and 2000s, Fedorov and colleagues discovered many results involving the receptivity of high speed flows. One can find a complete bibliography in Refs. 18–20.

Particularly, this spatial analysis of the 2D instability modes in hypersonic flows revealed the following: (1) in the region of the leading edge, two discrete modes, Mode F and Mode S (we use Fedorov's[18] terminology), are synchronized with fast and slow acoustic waves, respectively; (2) at a downstream location, Mode F is synchronized with the entropy and vorticity waves; and (3) further downstream, Mode F and Mode S could also become synchronized.[21] It is important to understand these features due to the role they may have in the transition process. Later on, similar features of Mode F and Mode S were seen in the 2D temporal problem.[14] One should note that for the 2D temporal problem, Mode F is the mode whose phase speed approaches that of the fast acoustic mode as $\alpha \to 0$, while Mode S is the mode whose phase speed approaches that of the slow acoustic mode as $\alpha \to 0$.

For the 3D initial-value problem, Mode F and Mode S were analyzed within the framework of the temporal stability theory in Ref. 15 for one particular choice of parameters, and the following features were revealed: (1) the synchronism of Mode S with acoustic waves at a streamwise wave number $\alpha \to 0$ is primarily two-dimensional; (2) at high angles of disturbance propagation, Mode F is no longer synchronized with entropy and vorticity waves; and (3) at high angles of disturbance propagation, the synchronism between Mode S and Mode F is not accompanied by a Mode S instability, and at even higher angles of disturbance propagation, Mode S and Mode F are not synchronized. These discrete modes were later analyzed within the framework of the spatial stability theory in Ref. 20, and similar results were found. A complete understanding of the features of the spectrum is needed to compute the inverse Fourier transform.

For clarity of the discussion, we will briefly review the previously solved initial-value problem for a 3D wave packet in a hypersonic boundary layer flow. Our objective is to consider the specific disturbance of an initial temperature spot. The receptivity to the temperature spot is found for both the 2D and 3D cases. The 2D inverse Fourier transform is computed for both Mode F and Mode S, and the computed inverse Fourier transform for Mode S is compared with an asymptotic approximation of the Fourier integral. The inverse Fourier transform for a prescribed value of the spanwise wave number is computed for Mode S, and this is compared with an asymptotic representation of the Fourier integral. Lastly, the 3D inverse Fourier transform is found using an asymptotic approximation.

II. PROBLEM FORMULATION

We consider a 3D parallel boundary layer flow of a calorically perfect gas. At the initial time $t=0$, a 3D localized disturbance is introduced into the flow. The problem is to describe the downstream evolution of the perturbation. The streamwise, normal, and spanwise spatial coordinates are given, respectively, by x, y, and z. Additionally, we denote u, v, and w to be, respectively, the streamwise, normal, and spanwise velocity disturbances, and θ, π, ρ, and μ to be, respectively, the temperature, pressure, density, and viscosity disturbances. Letting

$$\boldsymbol{A} = (u, \partial u/\partial y, v, \pi, \theta, \partial\theta/\partial y, w, \partial w/\partial y)^T \tag{1}$$

be the disturbance vector function, where "T" stands for "transpose," it is possible to rewrite the system of linearized, dimensionless governing equations (continuity equation, x, y, and z momentum equations, and energy equation) in the following matrix operator form:

$$\frac{\partial}{\partial y}\left(\boldsymbol{L}_0\frac{\partial \boldsymbol{A}}{\partial y}\right) + \frac{\partial \boldsymbol{A}}{\partial y} = \boldsymbol{H}_{10}\frac{\partial \boldsymbol{A}}{\partial t} + \boldsymbol{H}_{11}\boldsymbol{A} + \boldsymbol{H}_2\frac{\partial \boldsymbol{A}}{\partial x} + \boldsymbol{H}_3\frac{\partial^2 \boldsymbol{A}}{\partial x\,\partial y} + \boldsymbol{H}_4\frac{\partial^2 \boldsymbol{A}}{\partial x^2} + \boldsymbol{H}_5\frac{\partial \boldsymbol{A}}{\partial z} + \boldsymbol{H}_6\frac{\partial^2 \boldsymbol{A}}{\partial x\,\partial z} + \boldsymbol{H}_7\frac{\partial^2 \boldsymbol{A}}{\partial y\,\partial z} + \boldsymbol{H}_8\frac{\partial^2 \boldsymbol{A}}{\partial z^2}, \tag{2}$$

where $\boldsymbol{L}_0$, $\boldsymbol{H}_{10}$, $\boldsymbol{H}_{11}$, $\boldsymbol{H}_2$, $\boldsymbol{H}_3$, $\boldsymbol{H}_4$, $\boldsymbol{H}_5$, $\boldsymbol{H}_6$, $\boldsymbol{H}_7$, and $\boldsymbol{H}_8$ are 8×8 matrices. The explicit form of these matrices can be found in Ref. 15. At the initial time $t=0$, the disturbance vector is denoted as

$$\boldsymbol{A}(x,y,z,0) = \boldsymbol{A}_0(x,y,z). \tag{3}$$

The boundary conditions are as follows:

$$\begin{aligned} &y = 0\text{: } u = v = w = \theta = 0, \\ &y \to \infty\text{: } |A_j| \to 0 \ (j = 1, \ldots, 8). \end{aligned} \tag{4}$$

These boundary conditions correspond to the no-slip condition and zero temperature disturbance on the wall, and all disturbances decaying to zero far outside the boundary layer.

III. SOLUTION OF THE INITIAL-VALUE PROBLEM

The problem is solved using a Fourier transform with respect to the streamwise coordinate, x, a Fourier transform with respect to the spanwise coordinate z, and a Laplace transform with respect to time t. The inverse Laplace transform of $\boldsymbol{A}_{p\alpha\beta}$, the solution of the transformed equations, is determined by poles (relevant to the discrete spectrum) and by branch cuts (relevant to the continuous spectrum). By integrating along an appropriate contour in the complex plane (see Ref. 15), the inverse Laplace transform can be

written as a sum of integrals along the sides, γ^+ and γ^-, of each branch cut and a sum of residues resulting from the poles; i.e.,

$$\boldsymbol{A}_{\alpha\beta} = -\frac{1}{2\pi i}\sum_m \left(\int_{\gamma_m^+} \boldsymbol{A}_{p\alpha\beta} e^{pt} dp + \int_{\gamma_m^-} \boldsymbol{A}_{p\alpha\beta} e^{pt} dp \right) + \sum_n \mathrm{Res}_n \left(\boldsymbol{A}_{p\alpha\beta} e^{pt} \right). \tag{5}$$

Details of the problem formulation and solution can be found in Ref. 15.

Discrete and continuous spectra

The behavior of the spectrum must be understood in order to compute the inverse Fourier transform. To illustrate features of the spectrum, we consider a boundary layer over a sharp cone at zero angle of attack. The length scale is $L^* = \sqrt{\mu_e^* x^* / \rho_e^* U_e^*}$ and the Reynolds number is $\mathrm{Re} = \sqrt{\rho_e^* U_e^* x^* / \mu_e^*}$, where U_e^*, ρ_e^*, and μ_e^* are, respectively, the streamwise mean velocity, density, and viscosity at the boundary layer edge, and "*" refers to a dimensional quantity. The coordinate x^* is measured from the front tip of the cone. Using the Lees-Dorodnitsyn transformation,[22] we solve the conical problem with boundary layer profiles for a flat plate. Accordingly, all conical results presented hereafter can be adjusted to the flat-plate boundary layer by dividing the parameters Re, α, β, and ω by $\sqrt{3}$. All numerical results are for the case of 2D mean flow. To maintain consistency with the 2D problem analyzed in Ref. 14, the following parameter values are chosen: M=5.6, Re=1219.5, Pr=0.7, and γ=1.4, with an adiabatic wall and stagnation temperature T_0=470 K, where M is the Mach number at the boundary layer edge, Pr is the Prandtl number, and γ is the specific heat ratio. These parameter values were initially chosen (in Ref. 14) to correspond with the experimental conditions of a Mach-6 wind tunnel at Purdue University.[23] With stagnation pressure p_0=10 bar, stagnation temperature T_0=470 K, free-stream Mach number M_∞=6, and a 5° half-angle cone, one can show that an edge Mach number M≈5.6 and Reynolds number Re≤2000 are reasonable parameter values.

Discrete modes are given by the poles' contribution to the inverse Laplace transform; i.e., the residues shown in Eq. (5). Continuous modes are given by the branch cuts' contribution to the inverse Laplace transform, i.e., the integrals shown in Eq. (5). There are three branch cuts associated with the continuous spectrum. These branch cuts are shown in Fig. 1 for α=0.2 and β=0.14, where α and β are, respectively, the streamwise and spanwise wave numbers. The upper and lower branch cuts correspond to fast and slow acoustic modes. The branch points of the upper and lower branch cuts represent fast and slow acoustic modes that travel downstream with the respective phase speeds $c = 1 \pm \sqrt{1+\beta^2/\alpha^2}/\mathrm{M}$. The horizontal branch cut in Fig. 1 consists of three overlapping modes (two vorticity modes and one entropy mode). The vorticity and entropy disturbances propagate downstream with a phase speed c=1. If an eigenvalue belongs to the discrete spectrum, then the associated eigenfunction decays exponentially outside the boundary layer ($y \to \infty$). Eigenfunctions associated with continuous modes oscillate outside the boundary layer. Details regarding the discrete spectrum and the various regions of the continuous spectrum can be found in Ref. 15.

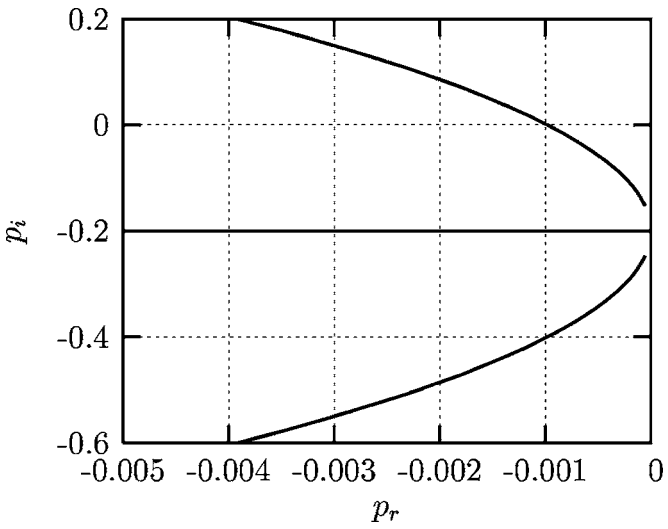

FIG. 1. Branch cuts of the continuous spectrum in the complex plane, $p=-i\omega$, for M=5.6, Re=1219.5, α=0.2, and β=0.14.

IV. BIORTHOGONAL SYSTEM OF EIGENFUNCTIONS

It is possible to express a solution of the initial-value problem as an expansion in the biorthogonal eigenfunction system $\{\boldsymbol{A}_\omega, \boldsymbol{B}_\omega\}$. The vector $\boldsymbol{A}_\omega$ is a solution of the direct problem, and the vector $\boldsymbol{B}_\omega$ is a solution of the adjoint problem.

Solutions of the direct and adjoint problems belong to the discrete and continuous spectra. The eigenfunction system $\{\boldsymbol{A}_\omega, \boldsymbol{B}_\omega\}$ has an orthogonality relation given as

$$\langle \boldsymbol{H}_{10}\boldsymbol{A}_\omega, \boldsymbol{B}_{\omega'} \rangle \equiv \int_0^\infty (\boldsymbol{H}_{10}\boldsymbol{A}_\omega, \boldsymbol{B}_{\omega'}) dy = \Gamma \Delta_{\omega,\omega'}, \tag{6}$$

where Γ is a normalization constant. $\Delta_{\omega,\omega'}$ is a Kronecker delta if either ω or ω' belong to the discrete spectrum. $\Delta_{\omega,\omega'} = \delta(\omega - \omega')$ is a Dirac delta function if both ω and ω' belong to the continuous spectrum.

It is possible to show that the inverse Laplace transform can be expressed as an expansion in the biorthogonal eigenfunction system:[15]

$$\boldsymbol{A}_{\alpha\beta}(y,t) = \sum_\nu c_\nu \boldsymbol{A}_{\alpha\beta\omega_\nu}(y) e^{-i\omega_\nu t} + \sum_j \int_0^\infty c_j(k) \boldsymbol{A}_{\alpha\beta\omega_j}(y) e^{-i\omega_j(k)t} dk, \tag{7}$$

where Σ_ν denotes a summation over the discrete spectrum and Σ_j denotes a summation over the continuous spectrum. Using the Fourier transform of the initial disturbance, $\boldsymbol{A}_{0\alpha\beta}$, as well as the orthogonality relation [Eq. (6)], one can find the coefficients c_ν and c_j. Further details regarding the biorthogonal system of eigenfunctions can be found in Ref. 15.

V. RECEPTIVITY TO A TEMPERATURE SPOT

As an example of a specific initial disturbance, we consider a temperature spot localized at a distance Y_0 from the wall. For the 3D initial-value problem, this disturbance will have the form

$$\theta(x,y,z) = \delta(x)\delta(y - Y_0)\delta(z) \quad \text{at } t = 0. \tag{8}$$

The orthogonality condition given by Eq. (6) allows one to determine the weights of the modes generated by the temperature spot. For Mode F and Mode S, the weight is given by

$$c(\alpha,\beta) = \frac{\langle \boldsymbol{H}_{10}\boldsymbol{A}_{0\alpha\beta}, \boldsymbol{B}_{\omega}\rangle}{\Gamma}, \tag{9}$$

where $\omega(\alpha,\beta)$ corresponds to the eigenvalue for the mode of interest. For a temperature spot of the form given by Eq. (8), it is possible to use the definition of $\boldsymbol{H}_{10}$ to obtain from Eq. (9) the expression

$$c(\alpha,\beta) = \frac{H_{10}^{35}(Y_0)\boldsymbol{B}_{\omega 3}(Y_0) + H_{10}^{65}(Y_0)\boldsymbol{B}_{\omega 6}(Y_0)}{\Gamma}, \tag{10}$$

with H_{10}^{ij} denoting the (i,j) element of matrix $\boldsymbol{H}_{10}$.

The coefficient $c(\alpha,\beta)$ depends on the normalization of the eigenfunction $\boldsymbol{A}_{\omega}$. However, the product $c(\alpha,\beta)\boldsymbol{A}_{\omega}$ is independent of the choice of normalization. We would like to normalize the eigenfunction so that the maximum value of u is 1. However, for our choice of parameters, there are two local maxima. We therefore choose to normalize the eigenfunction so that the value of the inner maximum is 1 (i.e., we normalize $\boldsymbol{A}_{\omega}$ as $u_{\max}$=inner maximum of $u(y)=1$). The normalized value of the outer maximum may be greater than 1. With this normalization, c is the amplitude of the maximum streamwise velocity component $u_{\max}$ associated with the appropriate mode.

As a limiting case, as $\beta \to 0$, one obtains the receptivity coefficient associated with the 2D initial-value problem.[14]

VI. INVERSE FOURIER TRANSFORM: 2D

The solution (before application of the two inverse Fourier transforms) is denoted as $\boldsymbol{A}_{\alpha\beta}$ and is given by Eq. (7). In the 2D case, the solution (before application of one inverse Fourier transform) is denoted as $\boldsymbol{A}_{\alpha}$ and will have a form similar to that of the 3D case. The 2D inverse Fourier transform is given by

$$\int_{-\infty}^{\infty} c(\alpha)\boldsymbol{A}_{\alpha}(\alpha,y)e^{i(\alpha x - \omega(\alpha)t)}d\alpha. \tag{11}$$

As an example, we consider the streamwise velocity component u of the disturbance vector $\boldsymbol{A}$. The transform we are therefore interested in is given as

$$\int_{-\infty}^{\infty} c(\alpha)u(\alpha,y)e^{i(\alpha x - \omega(\alpha)t)}d\alpha, \tag{12}$$

where the coefficient $c(\alpha)$ is, for this example, the amplitude of the maximum streamwise velocity component $u_{\max}$. Expression (12) is transformed using a symmetry argument. Using the direct and complex conjugate matrix operator

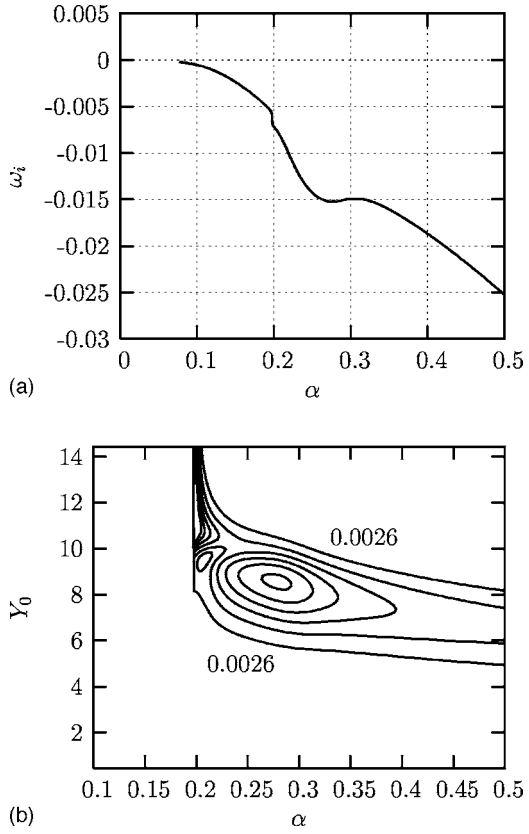

FIG. 2. (a) Imaginary part of the eigenvalue for Mode F and (b) contours of $u_{\max}$ at $t=0$ generated by α components of the temperature spot located at Y_0. The contour levels in (b) range from 0.0026 to 0.0156 in increments of 0.0026.

equations, when α is replaced by $-\alpha$, i.e., when $\alpha \to -\alpha$, it can be shown that $\omega \to -\bar{\omega}$, $c \to \bar{c}$, and $u \to \bar{u}$, where the overbar stands for complex conjugate. Therefore, (12) can be rewritten as

$$\int_{-\infty}^{\infty} c(\alpha)u(\alpha,y)e^{i(\alpha x - \omega(\alpha)t)}d\alpha \tag{13a}$$

$$= 2\int_{0}^{\infty} \text{Real}\{c(\alpha)u(\alpha,y)e^{i(\alpha x - \omega(\alpha)t)}\}d\alpha. \tag{13b}$$

In the computation, we ignore the factor of 2. For the purpose of analysis, the Mode F and Mode S wave packets are considered separately.

A. Mode F

Figure 2(a) shows the imaginary part of the eigenvalue ω_i for Mode F. Figure 2(b) shows the maximum streamwise velocity amplitude, $u_{\max}$, at $t=0$ for Mode F, which is generated by α components of the temperature spot located at varying normal distances Y_0 from the wall. One can see from Fig. 2(b) that there is little to no receptivity to a temperature spot located at $Y_0 < 5$ and $Y_0 > 11$.

The integral given by (13b) is numerically computed from $\alpha=0.1$ to $\alpha=0.5$. We were unable to calculate the Mode F eigenvalues below $\alpha \approx 0.08$ [Fig. 2(a)]. However, for a finite time, the input into the integral for $\alpha < 0.1$ is not sig-

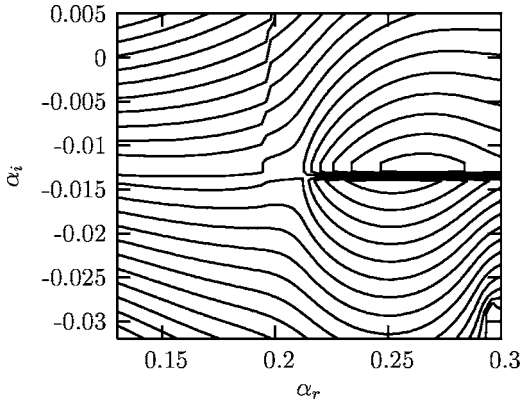

FIG. 3. Contours of ω_i in the complex α plane. The contours range from −0.0298 at the bottom of the figure to 0.0028 at the top of the figure in increments of 0.0015.

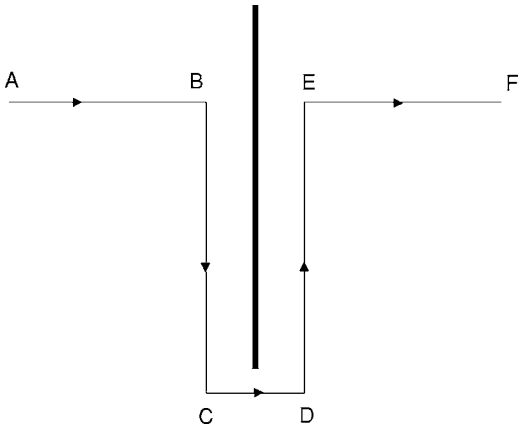

FIG. 4. Schematic of an integration path around the branch cut.

nificant since the receptivity coefficient, $u_{\max}$, is close to 0 for this range of α [Fig. 2(b)]. Beyond this finite time, the main input into the integral will come from the piece of Mode F with the largest values of ω_i (as $\alpha \to 0$), and this range of α should be considered.

Figure 2(b) also shows that the largest values of $u_{\max}$ occur near $\alpha \approx 0.27$. This fact, coupled with the fact that Mode F is decaying everywhere, suggests that there will not be much input into the integral for $\alpha > 0.5$ if a sufficiently large time t is chosen.

There is a synchronism between Mode F and the entropy and vorticity modes. As the discrete mode coalesces with the continuous spectrum from one side of the branch cut, it reappears on the other side at another point. This leads to the jump in ω_i seen in Fig. 2(a).

Figure 3 shows contours of ω_i in the complex α plane. One can see the jumps in ω_i along a nearly vertical line. As (13b) is integrated from $\alpha = 0.1$ to $\alpha = 0.5$, we must consider the continuous spectrum along with Mode F at the point of coalescence. To make the analysis less complicated, we analytically continue the path of integration into the complex α plane in order to avoid the discontinuities associated with the coalescence of Mode F with the continuous spectrum. Therefore, the computed result is obtained using only Mode F. However, had we considered the sum of Mode F and the continuous spectrum and integrated along the real α axis, we would obtain the same result. Figure 4 is a schematic of an appropriate integration path. Due to the analyticity of the function being integrated, the result should be independent of the path of integration.

Using $Y_0 = 8.9$ (the edge of the boundary layer is located at $y \approx 10$), $t = 50$ and the integration path, Path 1, (13b) is integrated. Using the letters found in Fig. 4 (with points A, B, E, and F located on the real axis), Path 1 is given explicitly as the following: At point A, $\alpha = 0.1$; at point B, $\alpha = 0.17$; at point C, $\alpha = 0.17 - 0.015i$; at point D, $\alpha = 0.2 - 0.015i$; at point E, $\alpha = 0.2$; and at point F, $\alpha = 0.5$.

The result is shown in Fig. 5(a) as contours of u in the x-y plane. To better illustrate the Mode F wave packet, Fig. 5(b) shows a slice of Fig. 5(a) taken at $y = 2.02$.

To illustrate the decay of the wave packet in time, (13b) is integrated again using Path 1 and $Y_0 = 8.9$ for $t = 200$. Figure 6 shows the result taken at the slice $y = 2.02$. When Fig. 6 is compared to Fig. 5(b), one sees that u is an order of magnitude smaller for $t = 200$ than for $t = 50$. This order of magnitude decrease in amplitude is consistent with $\omega_i \approx -0.015$ [Fig. 2(a)]. Additionally, the wave packet is seen to have moved downstream with the increase in time. By comparison of Fig. 6 to Fig. 5(b), one can also estimate the Mode F wave packet group velocity to be $\partial \omega_r / \partial \alpha \approx 0.65$. One can see from

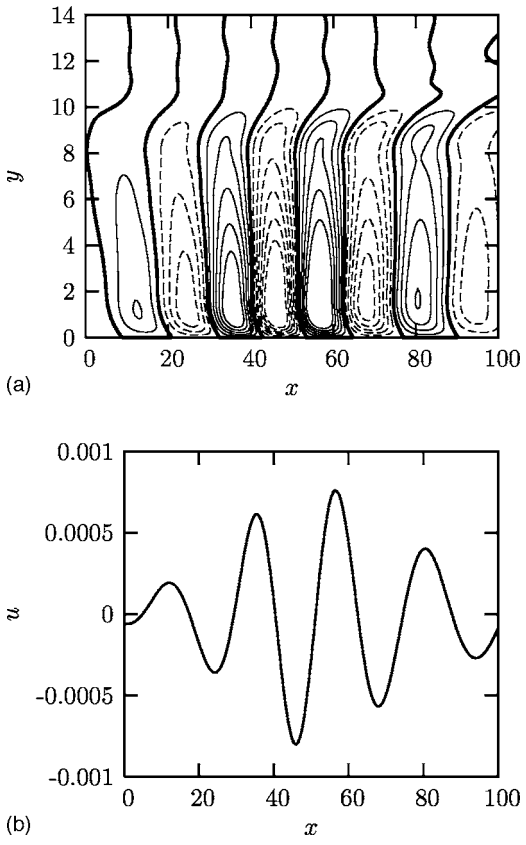

FIG. 5. (a) Contours of u in the x-y plane and (b) streamwise velocity disturbance, u, at $y = 2.02$ for $t = 50$. The contour levels in (a) are spaced in increments of 0.0001. The solid contours are positive; the dashed contours are negative; the bold contours are 0.

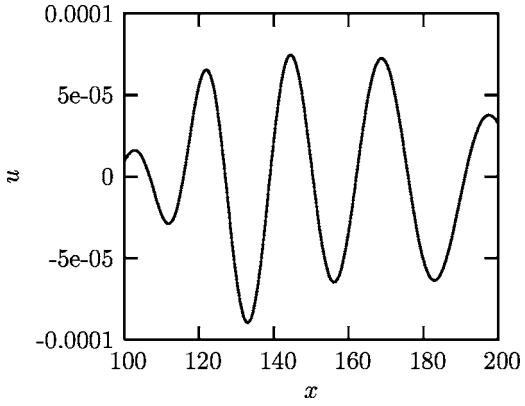

FIG. 6. Streamwise velocity disturbance u at $y=2.02$ for $t=200$.

Fig. 10 [Mode F eigenvalue curve for $\beta=0.0001$ (2D)] in Ref. 15 that the group velocity estimate is very reasonable.

For the two times considered, we expect the main input into the integral to come from the receptivity coefficient. Figure 7 shows the amplitude spectrum for Mode F for both $t=50$ and $t=200$. This figure shows that the main input for both $t=50$ and $t=200$ occurs at an α value that corresponds favorably with the maximum values of $u_{\max}$ for a temperature spot located at $Y_0=8.9$ [Fig. 2(b)]. As time increases, the main input to the integral will no longer come from the receptivity coefficient, but rather from the $e^{-i\omega(\alpha)t}$ component of the integrand at low α. Therefore, we expect the amplitude peak to be located at low values of α for large times. For $t=200$, Fig. 7 shows that the amplitude peak has begun this shift to lower values of α. In addition, Fig. 7 clearly shows the decay of Mode F in time.

To ensure that these results are independent of the choice of path of integration, the results shown for $Y_0=8.9$ at $t=50$ using Path 1 are compared with results found using three other paths of integration. Using the letters found in Fig. 4, Paths 2, 3, and 4 are given as follows:

Path 2. At point A, $\alpha=0.1$. At point B, $\alpha=0.15$. At point C, $\alpha=0.15-0.015i$. At point D, $\alpha=0.2-0.015i$. At point E, $\alpha=0.2$, and at point F, $\alpha=0.5$.

Path 3. At point A, $\alpha=0.1$. At point B, $\alpha=0.15$. At point C, $\alpha=0.15-0.015i$. At point D, $\alpha=0.21-0.015i$. At point E, $\alpha=0.21$, and at point F, $\alpha=0.5$.

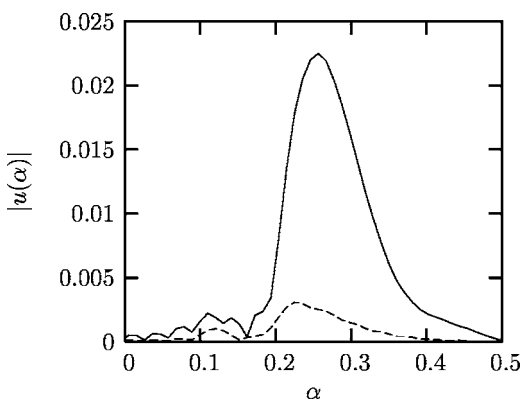

FIG. 7. Amplitude spectrum of Mode F for $t=50$ (solid line) and $t=200$ (dashed line).

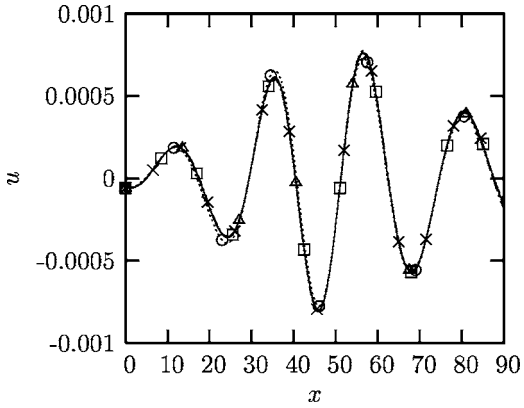

FIG. 8. Streamwise velocity disturbance u at $y=2.02$ for $t=50$ for 4 paths of integration. The Path 1 result is denoted with "cross" markers; the Path 2 result with "square" markers; the Path 3 result with "circle" markers; the Path 4 result with "triangle" markers.

Path 4. At point A, $\alpha=0.1$. At point B, $\alpha=0.17$. At point C, $\alpha=0.17-0.031i$. At point D, $\alpha=0.2-0.031i$. At point E, $\alpha=0.2$, and at point F, $\alpha=0.5$.

To compare the results, Fig. 8 shows the wave packet at the slice $y=2.02$ for each choice of integration path.

There is good agreement between the results obtained using the four different integration paths. A portion of each path of integration passes through a region of the complex α plane where $\alpha_i<0$. This leads to numerical error associated with growth from the $e^{i\alpha x}$ term in the integrand. Since Path 3 has a longer portion of its path in the negative complex α plane, this phenomena explains why the Path 3 result differs from the other three results (this deviation is difficult to see at the scale used for Fig. 8).

B. Mode S

Figure 9(a) shows the imaginary part of the eigenvalue ω_i for Mode S. Figure 9(b) shows the maximum streamwise velocity amplitude, $u_{\max}$, at $t=0$ for Mode S, which is generated by α components of the temperature spot located at varying normal distances Y_0 from the wall.

The integral given by (13b) is numerically computed from $\alpha=0.1$ to $\alpha=0.5$. The greatest input into the integral will be from the region of $\alpha\approx0.2$ to $\alpha\approx0.3$. It is in this region that the receptivity coefficient $u_{\max}$ is the highest, and it is also in this region where ω_i attains its largest value. Beyond $\alpha=0.5$, Mode S is decaying, so that for sufficiently large times, there will not be significant input into the integral for $\alpha>0.5$.

Unlike the Mode F case, there is no need to deform the path of integration to compute the Mode S inverse Fourier transform. The result for $Y_0=8.9$ at $t=500$ is shown in Fig. 10(a) as contours of u in the x-y plane. To better illustrate the Mode S wave packet, Fig. 10(b) shows a slice of Fig. 10(a) taken at $y=2.02$.

We expect that the main input into the integral will come from the Gaussian shaped growth portion of the Mode S eigenvalue plot [Fig. 9(a)]. Figure 11 shows the amplitude spectrum of Mode S for $t=500$. This figure shows that the

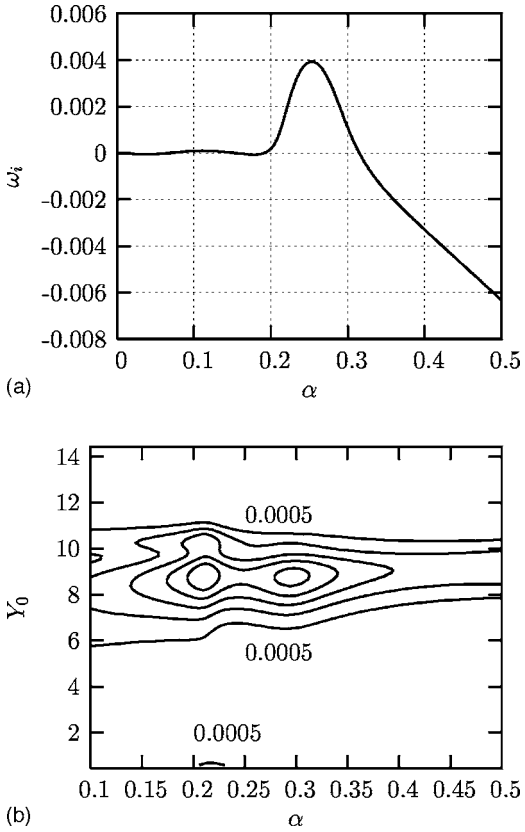

FIG. 9. (a) Imaginary part of the eigenvalue for Mode S and (b) contours of u_{max} at $t=0$ generated by α components of the temperature spot located at Y_0. The contour levels in (b) range from 0.0005 to 0.0025 in increments of 0.0005.

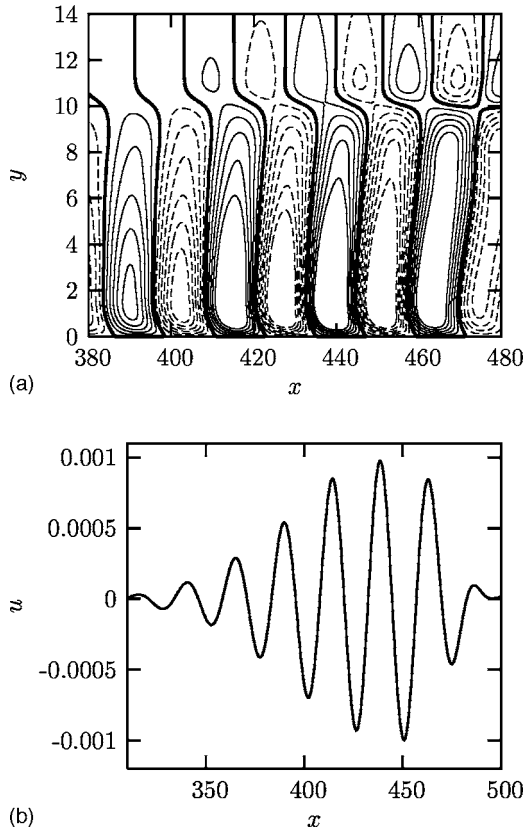

FIG. 10. (a) Contours of u in the x-y plane and (b) streamwise velocity disturbance u at $y=2.02$ for $t=500$. The contour levels in (a) are spaced in increments of 0.0001. The solid contours are positive; the dashed contours are negative; the bold contours are 0.

main input occurs at an α value that compares favorably with the location of the Gaussian peak [Fig. 9(a)].

1. Asymptotic approximation with Taylor series expansion of $\omega(\alpha)$

Because the eigenvalue plot for Mode S contains a region where $\omega_i > 0$, the Mode S wave packet, unlike the Mode F wave packet, will grow in time (and downstream). It is useful to compare the Mode S computed inverse Fourier transform with an asymptotic approximation of the Fourier integral.

The development of 2D and 3D wave packets comprised of spatially growing discrete modes for incompressible boundary layer flows (parallel and nonparallel) has been considered previously by Gaster.[24–26] In particular, Gaster used the method of steepest descent to find the asymptotic representation of integrals of the form given by (13b). Starting with (13b), we have the following:

$$\int_{-\infty}^{\infty} c(\alpha)u(\alpha,y)e^{i(\alpha x-\omega(\alpha)t)}d\alpha = \int_{-\infty}^{\infty} c(\alpha)u(\alpha,y)e^{it(\alpha(x/t)-\omega(\alpha))}d\alpha. \quad (14)$$

Assuming that the saddle point lies near the point α_{max}, we approximate $\omega(\alpha)$ as

$$\omega(\alpha) \approx \omega_{max} + (\alpha-\alpha_{max})\left(\frac{\partial\omega}{\partial\alpha}\right)_{max} + \frac{1}{2}(\alpha-\alpha_{max})^2\left(\frac{\partial^2\omega}{\partial\alpha^2}\right)_{max}, \quad (15)$$

where $(\partial\omega/\partial\alpha)_{max}$ is real valued. To find the saddle point, α^*, at a prescribed x/t, we let $\phi(\alpha)=\alpha x/t-\omega(\alpha)$ and derive the following:

$$\left(\frac{\partial\phi}{\partial\alpha}\right)^* = \frac{x}{t} - \left(\frac{\partial\omega}{\partial\alpha}\right)_{max} - (\alpha^*-\alpha_{max})\left(\frac{\partial^2\omega}{\partial\alpha^2}\right)_{max} = 0. \quad (16)$$

Solving for α^*, one obtains

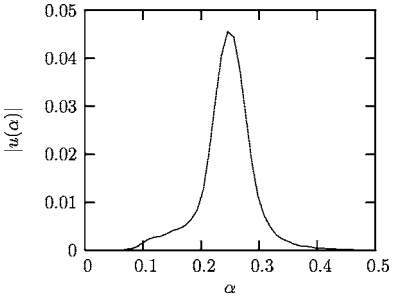

FIG. 11. Amplitude spectrum of Mode S for $t=500$.

$$\alpha^* = \alpha_{\max} + \frac{\frac{x}{t} - \left(\frac{\partial\omega}{\partial\alpha}\right)_{\max}}{\left(\frac{\partial^2\omega}{\partial\alpha^2}\right)_{\max}}. \tag{17}$$

Equation (17) can be rewritten as

$$\alpha^* = \alpha_{\max} + \frac{x - x_{\max}}{t\left(\frac{\partial^2\omega}{\partial\alpha^2}\right)_{\max}}, \tag{18}$$

where $x_{\max} = t(\partial\omega/\partial\alpha)_{\max}$.

Expression (14) can now be rewritten as

$$c(\alpha^*)u(\alpha^*,y)\int_L e^{it[\phi(\alpha^*)+(1/2)(\alpha-\alpha_{\max})^2\phi''(\alpha^*)]}d\alpha \tag{19a}$$

$$= c(\alpha^*)u(\alpha^*,y)\sqrt{-\frac{2\pi}{it\phi''(\alpha^*)}}e^{it\phi(\alpha^*)} \tag{19b}$$

$$= c(\alpha^*)u(\alpha^*,y)\sqrt{\frac{2\pi}{it\left(\frac{\partial^2\omega}{\partial\alpha^2}\right)_{\max}}}e^{it\phi(\alpha^*)}, \tag{19c}$$

where L is the contour of integration that has been deformed to pass through the saddle point, the prime ($'$) symbol denotes differentiation with respect to α, and $\phi'' = -\partial^2\omega/\partial\alpha^2$.

After substitution of α^* into (19c), the asymptotic representation of the original Fourier integral is given as

$$c(\alpha^*)u(\alpha^*,y)\sqrt{\frac{2\pi}{it\left(\frac{\partial^2\omega}{\partial\alpha^2}\right)_{\max}}} \times\exp\left(i\alpha_{\max}x + \frac{i(x-x_{\max})^2}{2t\left(\frac{\partial^2\omega}{\partial\alpha^2}\right)_{\max}} - i\omega_{\max}t\right). \tag{20}$$

Actually, the use of a second-order Taylor series expansion of $\omega(\alpha)$ within the framework of the method of steepest descent is equivalent to Gaster's[24,25] Gaussian model for a Fourier integral.

Using numerical results, the various quantities found in (20) can be determined. They are

$$\alpha_{\max} = 0.254, \quad \omega_{\max} = 0.2342 + 0.0039i,$$

$$\left(\frac{\partial\omega}{\partial\alpha}\right)_{\max} = 0.86, \quad \left(\frac{\partial^2\omega}{\partial\alpha^2}\right)_{\max} = -0.2034 - 3.6431i.$$

Additionally, $c(\alpha^*)u(\alpha^*,y)$, the receptivity coefficient multiplied by the eigenfunction at the saddle point for the slice $y=2.02$ is $0.00174-0.0011i$.

These values can be used to compare the computed inverse Fourier transform with the asymptotic approximation of the transform. Because we have used (13b) without the factor of 2 to compute the inverse Fourier transform, we will compare the computational result with the real part of the asymptotic approximation given by (20). Though we expect good agreement between the two methods, especially for large times, there may be some differences between the "exact" result found numerically and the "approximate" result found with the method of steepest descent.

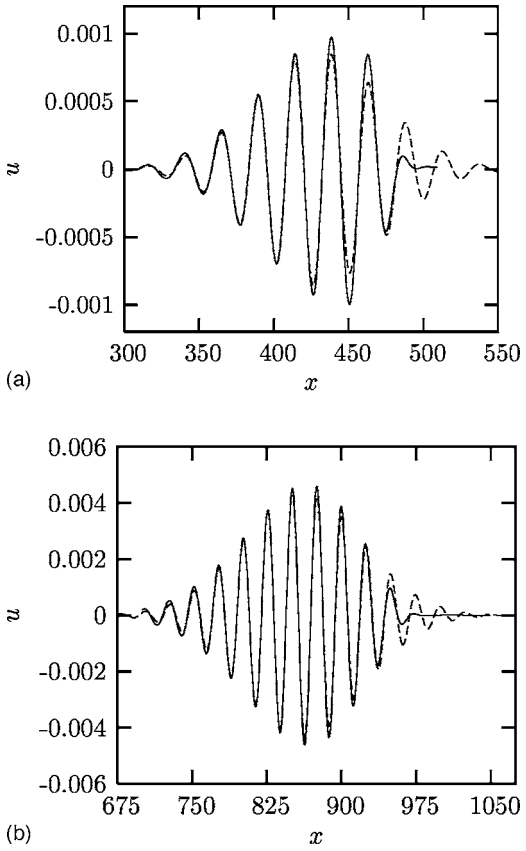

FIG. 12. Comparison of computed integral (solid line) with the asymptotic approximation [using second-order Taylor series expansion of $\omega(\alpha)$] (dashed line) for (a) $t=500$ and (b) $t=1000$.

Figure 12(a) compares the wave packet found for $Y_0=8.9$ and $t=500$ at the slice $y=2.02$ with the asymptotic approximation at $t=500$ given by (20) using the values given above. Figure 12(b) shows a similar comparison for $t=1000$. One can see that as the time increases, the wave packet spreads out as it moves downstream. Furthermore, the amplitude of the perturbation increases with time. By comparing Fig. 12(a) to Fig. 12(b), one can estimate the Mode S wave packet group velocity to be $\partial\omega_r/\partial\alpha \approx 0.8$. This estimate is consistent with the group velocity value $(\partial\omega/\partial\alpha)_{\max}=0.86$.

Overall, the asymptotic representation provides a good approximation to the computed wave packet. However, the "tails" of the two wave packets do not agree very well. This is particularly true for the front edge of the wave packet.

2. Asymptotic approximation with numerical computation of the saddle point

In an attempt to improve the asymptotic approximation of the wave packet at the "tails" of the wave packet, we numerically compute the location of the saddle point. To find the saddle point, α^*, at a prescribed x/t, we let $\phi(\alpha)=\alpha x/t - \omega(\alpha)$ and derive the following:

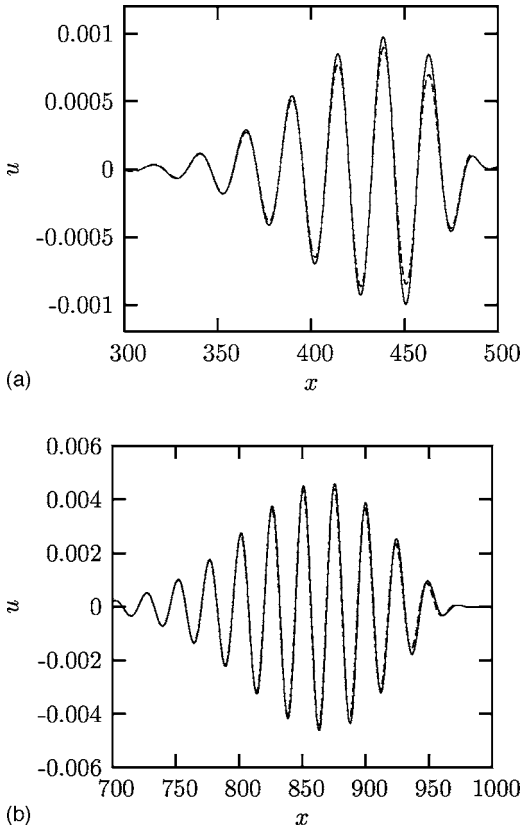

FIG. 13. Comparison of computed integral (solid line) with the asymptotic approximation (using numerically computed saddle point values) (dashed line) for (a) $t=500$ and (b) $t=1000$.

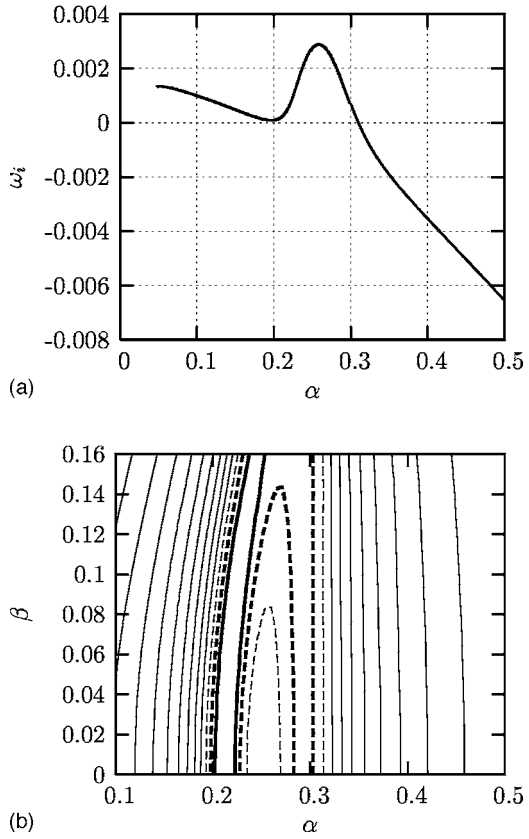

FIG. 14. (a) Imaginary part of the eigenvalue for Mode S for $\beta=0.1001$ and (b) contours of $c(\alpha,\beta)u$ at $y=2.02$ at $t=0$ generated by α and β components of a temperature spot located at $Y_0=8.9$. The contour levels in (b) increase in increments of 0.0002, beginning with 0.0004 on the left side of the figure and 0.0006 on the right side of the figure. The dashed contour is 0.0022, the bold dashed contour is 0.0024 and the bold solid contour is 0.0026.

$$\left(\frac{\partial\phi}{\partial\alpha}\right)^* = \frac{x}{t} - \frac{\partial\omega}{\partial\alpha} = 0. \tag{21}$$

Therefore, the following relationships must be satisfied at α^*:

$$\frac{x}{t} = \frac{\partial\omega_r}{\partial\alpha} \quad \text{and} \quad 0 = \frac{\partial\omega_i}{\partial\alpha}. \tag{22}$$

Using the method of steepest descent, the asymptotic representation of the inverse Fourier transform is given as

$$c(\alpha^*)u(\alpha^*,y)\sqrt{\frac{2\pi}{it\left(\frac{\partial^2\omega}{\partial\alpha^2}\right)^*}}\exp(i\alpha^* x - i\omega^* t). \tag{23}$$

[Note that (23) is the same as (20) with $x=x_{\max}$ and all of the "max" values replaced by "saddle point (*)" values.]

Using Eq. (22), α^*, ω^*, and $(\partial^2\omega/\partial\alpha^2)^*$ are calculated. Figure 13(a) compares the exact computed wave packet found for $Y_0=8.9$ and $t=500$ at the slice $y=2.02$ with the asymptotic approximation at $t=500$ given by (23) using the saddle point values. Figure 13(b) shows a similar comparison for $t=1000$. There is now excellent agreement across the entire wave packet for both choices of time.

VII. INVERSE FOURIER TRANSFORM-3D FOR FIXED SPANWISE WAVE NUMBER

For the streamwise velocity disturbance u [of $\boldsymbol{A}_{\alpha\beta}$ given by Eq. (7)], the 3D inverse Fourier transform is given by

$$\int_{-\infty}^{\infty}\int_{-\infty}^{\infty} c(\alpha,\beta)u(\alpha,\beta,y)e^{i[\alpha x+\beta z-\omega(\alpha,\beta)t]}d\alpha d\beta. \tag{24}$$

Integration with respect to α for a prescribed β leads to

$$e^{i\beta z}\int_{-\infty}^{\infty} c(\alpha,\beta)u(\alpha,\beta,y)e^{i[\alpha x-\omega(\alpha,\beta)t]}d\alpha. \tag{25}$$

As for the 2D case, the integral of (25) can be transformed using a symmetry argument to an integral over the positive α half-plane. As before, for the purpose of computation, we ignore the factor of 2.

Figure 14(a) shows the imaginary part of the eigenvalue ω_i for Mode S for $\beta=0.1001$. Figure 14(b) shows for Mode S at $t=0$ the maximum streamwise velocity amplitude $u_{\max}$ multiplied by the value of the eigenfunction at $y=2.02$, which is generated by α and β components of the temperature spot located at the distance $Y_0=8.9$ from the wall.

The inverse Fourier transform given by (25) is numerically computed from $\alpha=0.1$ to $\alpha=0.5$ with $\beta=0.1001$ and $z=0$. Even though $\omega_i>0$ for $\alpha<0.1$, the receptivity coefficient [Fig. 14(b)] is near 0 in this region. The greatest input into the integral will be from the region of $\alpha\approx0.2$ to $\alpha\approx0.3$. It is in this region that the receptivity coefficient $u_{\max}$ is the largest, and it is also in this region where ω_i

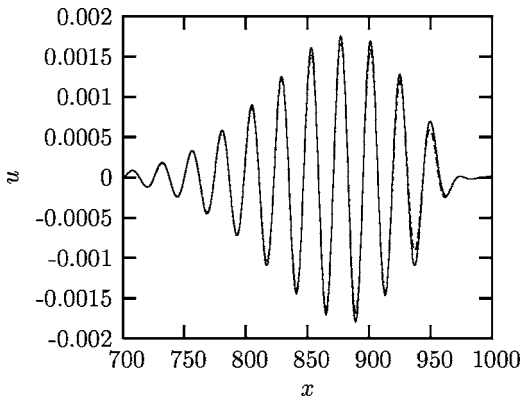

FIG. 15. Comparison of computed integral (solid line) with the asymptotic approximation (using numerically computed saddle point values) (dashed line) for $\beta=0.1001$, $z=0$, and $t=1000$.

attains its largest value. Beyond $\alpha=0.5$, Mode S is decaying, so that for sufficiently large times, there will not be significant input into the integral for $\alpha>0.5$.

Using the method of steepest descent, the asymptotic approximation of the inverse Fourier transform for a prescribed spanwise wave number β is given as

$$c(\alpha^*,\beta)u(\alpha^*,\beta,y)\sqrt{\frac{2\pi}{it\left(\frac{\partial^2\omega}{\partial\alpha^2}\right)^*}}\exp(i\beta z)\times\exp(i\alpha^* x - i\omega^* t). \tag{26}$$

By numerically computing the saddle point quantities α^*, ω^*, and $(\partial^2\omega/\partial\alpha^2)^*$, and using the fact that $c(\alpha^*,\beta)u(\alpha^*,\beta,y)$, the receptivity coefficient multiplied by the eigenfunction at the saddle point for the slice $y=2.02$ is $0.00159-0.00126i$, one can use (26) to find the asymptotic representation of the Fourier integral [as with the 2D case, the real part of (26) is taken for the purpose of comparison with the computed result].

Figure 15 compares the wave packet computed for $\beta=0.1001$, $z=0$, $Y_0=8.9$, and $t=1000$ at the slice $y=2.02$ with the asymptotic approximation at $t=1000$ given by (26). There is good agreement across the entire wave packet.

VIII. INVERSE FOURIER TRANSFORM-3D

It was shown in Sec. VI that it was necessary to deform the path of integration of the 2D inverse Fourier transform for Mode F, but not for Mode S. Each inversion of the Fourier integral must be accompanied by an analysis of the spectrum to find a suitable integration path. In order to perform the double integration of the 3D inverse Fourier transform, it is again necessary to understand the features of the spectrum so that an appropriate path of integration is used. Due to the complexities associated with the 3D spectrum, we will use an asymptotic approximation of the Fourier integral to compute the 3D wave packets.

For the streamwise velocity disturbance u the 3D inverse Fourier transform is given by (24). As in the 2D case, (24) can be transformed using a symmetry argument. Using the direct and complex conjugate matrix operator equations, when α is replaced by $-\alpha$, i.e., when $\alpha\to-\alpha$, it can be shown that $\beta\to-\beta$, $\omega\to-\bar{\omega}$, $c\to\bar{c}$, and $u\to\bar{u}$, where the overbar stands for complex conjugate. Therefore, (24) can be rewritten as

$$\int_{-\infty}^{\infty}\int_{-\infty}^{\infty}c(\alpha,\beta)u(\alpha,\beta,y)e^{i[\alpha x+\beta z-\omega(\alpha,\beta)t]}d\alpha d\beta = 2\int_0^{\infty}\int_0^{\infty}\mathrm{Real}\{c(\alpha,\beta)u(\alpha,\beta,y)e^{i[\alpha x+\beta z-\omega(\alpha,\beta)t]}\}d\alpha d\beta \tag{27a}$$

$$+2\int_0^{\infty}\int_0^{\infty}\mathrm{Real}\{c(\alpha,-\beta)u(\alpha,-\beta,y)\times e^{i[\alpha x-\beta z-\omega(\alpha,-\beta)t]}\}d\alpha d\beta. \tag{27b}$$

As before, the factor of 2 will be ignored.

At a first glance of (27b), it is tempting to think that there are two saddle points. The first saddle point, associated with the first double integral, must satisfy the following relations:

$$\frac{x}{t}=\frac{\partial\omega_r(\alpha,\beta)}{\partial\alpha}\quad\text{and}\quad 0=\frac{\partial\omega_i(\alpha,\beta)}{\partial\alpha},\qquad \frac{z}{t}=\frac{\partial\omega_r(\alpha,\beta)}{\partial\beta}\quad\text{and}\quad 0=\frac{\partial\omega_i(\alpha,\beta)}{\partial\beta}. \tag{28}$$

The second saddle point, associated with the second double integral, must satisfy the following relations:

$$\frac{x}{t}=\frac{\partial\omega_r(\alpha,-\beta)}{\partial\alpha}\quad\text{and}\quad 0=\frac{\partial\omega_i(\alpha,-\beta)}{\partial\alpha},\qquad \frac{z}{t}=\frac{\partial\omega_r(\alpha,-\beta)}{\partial\beta}\quad\text{and}\quad 0=\frac{\partial\omega_i(\alpha,-\beta)}{\partial\beta}. \tag{29}$$

Using the symmetry transformations along with properties of complex conjugation, it can be shown that Eq. (29) can be rewritten as

$$\frac{x}{t}=-\frac{\partial\omega_r(\alpha,\beta)}{\partial\alpha}\quad\text{and}\quad 0=\frac{\partial\omega_i(\alpha,\beta)}{\partial\alpha},\qquad \frac{z}{t}=\frac{\partial\omega_r(\alpha,\beta)}{\partial\beta}\quad\text{and}\quad 0=\frac{\partial\omega_i(\alpha,\beta)}{\partial\beta}. \tag{30}$$

However, it can be shown numerically that no saddle point satisfies the relations given in Eq. (30), unless $x=0$ and $z=0$. Therefore, there is only one saddle point, and it is associated with the first double integral of (27b).

We follow Gaster[26] to find the asymptotic representation of the 3D inverse Fourier transform. For a fixed β, the Fourier integral becomes

$$\int_{-\infty}^{\infty} e^{i\beta z} \int_{-\infty}^{\infty} e^{it[\alpha(x/t)-\omega(\alpha,\beta)]} d\alpha d\beta. \tag{31}$$

The asymptotic representation of the inner integral in (31) is known from the 2D case, and substitution of this representation leads to the following:

$$\sqrt{\frac{2\pi}{i}} \int_{-\infty}^{\infty} \frac{e^{it\{\alpha^*(\beta)(x/t)+\beta(z/t)-\omega[\alpha^*(\beta),\beta]\}}}{\sqrt{t\dfrac{\partial^2\omega}{\partial\alpha^2}(\alpha^*,\beta)}} d\beta. \tag{32}$$

If we let

$$\phi(\alpha^*,\beta) = i\left\{\alpha^*(\beta)\frac{x}{t} + \beta\frac{z}{t} - \omega[\alpha^*(\beta),\beta]\right\}, \tag{33}$$

and expand ϕ about β^* so that

$$\phi(\alpha^*,\beta) \approx i\left[\phi(\alpha^*,\beta^*) + \frac{(\beta-\beta^*)^2}{2}\phi''(\alpha^*,\beta^*)\right], \tag{34}$$

then (31) can be written as

$$\sqrt{\frac{2\pi}{it}} \frac{e^{it[\alpha^* x+\beta^* z-\omega(\alpha^*,\beta^*)]}}{\sqrt{\dfrac{\partial^2\omega}{\partial\alpha^2}(\alpha^*,\beta^*)}} \times \int_{-\infty}^{\infty} \exp\left\{it\frac{(\beta-\beta^*)^2}{2}\left[\frac{\partial^2\omega}{\partial\beta^2} + 2\frac{\partial^2\omega}{\partial\alpha\,\partial\beta}\left(\frac{\partial\alpha}{\partial\beta}\right) + \frac{\partial^2\omega}{\partial\alpha^2}\left(\frac{\partial\alpha}{\partial\beta}\right)^2\right]^*\right\} d\beta \tag{35a}$$

$$= \frac{2\pi}{it} \frac{e^{it[\alpha^* x+\beta^* z-\omega(\alpha^*,\beta^*)]}}{\sqrt{\left[\dfrac{\partial^2\omega}{\partial\alpha^2}\dfrac{\partial^2\omega}{\partial\beta^2} - \left(\dfrac{\partial^2\omega}{\partial\alpha\,\partial\beta}\right)^2\right]^*}}. \tag{35b}$$

The asymptotic representation of the inverse Fourier transform given by (35b) can be derived more generally using a transformation of variables.[27,28] Starting with (24) with ϕ given as $\phi(\alpha,\beta)=\alpha x+\beta z-\omega(\alpha,\beta)t$, we approximate ϕ as

$$\phi(\alpha,\beta) \approx \phi^* + \frac{(\alpha-\alpha^*)^2}{2}\phi^*_{\alpha\alpha} + (\alpha-\alpha^*)(\beta-\beta^*)\phi^*_{\alpha\beta} + \frac{(\beta-\beta^*)^2}{2}\phi^*_{\beta\beta}, \tag{36}$$

where the α and β subscripts refer to first and second partial derivatives, respectively.

Using the change of variables

$$g = (\alpha-\alpha^*), \quad h = (\beta-\beta^*), \qquad \xi = g + \frac{\phi_{\alpha\beta}}{\phi_{\alpha\alpha}}h, \quad \eta = h, \tag{37}$$

(24) is transformed to the following:

$$\int_{-\infty}^{\infty}\int_{-\infty}^{\infty} \exp\left\{\frac{t}{2}\left[\phi_{\alpha\alpha}\xi^2 + \frac{(\phi_{\alpha\alpha}\phi_{\beta\beta}-\phi_{\alpha\beta}^2)}{\phi_{\alpha\alpha}}\eta^2\right]\right\} d\xi\, d\eta. \tag{38}$$

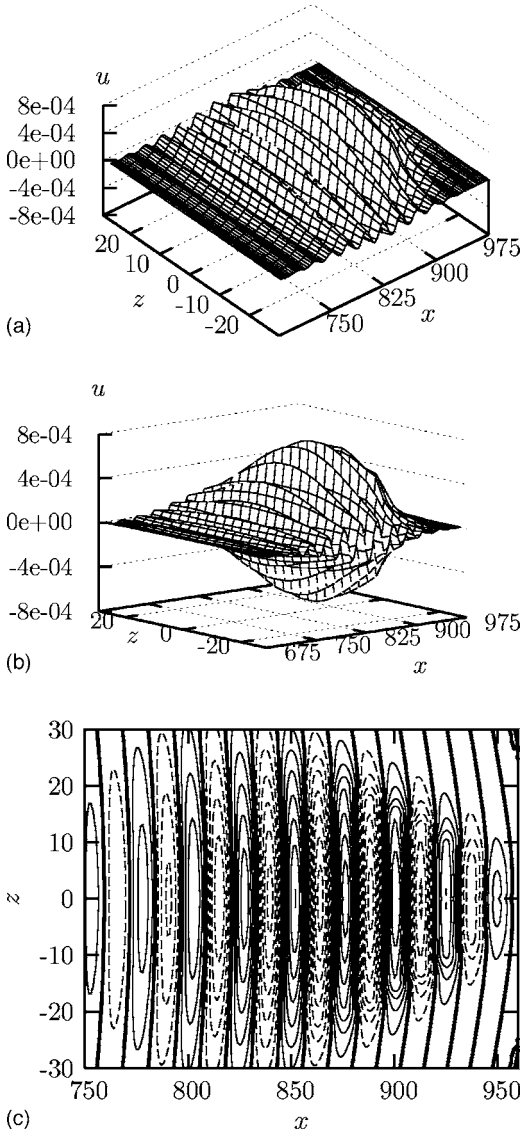

FIG. 16. (a) Surface (view 1), (b) surface (view 2), and (c) contours of u for $y=2.02$, $Y_0=8.9$, and $t=1000$. The contour levels in (c) are spaced in increments of 0.0001. The solid contours are positive; the dashed contours are negative; the bold contours are 0.

The integral given in (38) is an iterated integral in which each integral is Gaussian. Evaluation of the iterated integral results in the asymptotic representation of the Fourier integral given by (35b).

The saddle point (α^*,β^*) and the various derivatives at the saddle point used in (35b) are numerically computed. Using the asymptotic approximation of the 3D inverse Fourier transform, the Mode S wave packet is calculated for $t=1000$. Figure 16(a) is a surface plot of the streamwise velocity disturbance u, taken at the slice $y=2.02$ for $Y_0=8.9$ and $t=1000$. Figure 16(b) is a rotation of Fig. 16(a) in order to see the underside of the wave packet. To have a clearer sense of the amplitude values, Fig. 16(c) shows contours of u for $y=2.02$, $Y_0=8.9$, and $t=1000$. It is clear from these figures that the wave packet is essentially 2D. Furthermore, it is possible to compare Figs. 16(a)–16(c) with Figs. 8(a)–8(c) of Ref. 29 (3D Mode S wave packet for $t=500$)

and see that the 3D Mode S wave packet group velocity is very similar to the 2D Mode S wave packet group velocity.

IX. CONCLUSIONS

The previously solved 2D and 3D initial-value problems were used along with features of the discrete and continuous spectrum for one set of parameters to study the evolution of wave packets for two discrete modes: Mode S and Mode F. The biorthogonal eigenfunction system provides a method for the determination of the weights of individual modes given a specific initial disturbance. Using the specific disturbance of an initial temperature spot, we computed the 2D inverse Fourier transform for both Mode F and Mode S. Additionally the 3D inverse Fourier transform was computed for a fixed value of spanwise wave number β.

As shown in Refs. 14 and 15, Mode F and Mode S are eigenvalue curves that correspond to the trajectory of poles in the complex p plane, while continuous modes correspond to branch cuts in the complex p plane. It is possible for various modes to be synchronized, and therefore it is crucial to fully understand the behavior of the spectrum before computing the inverse Fourier transform. For the 2D case, due to the synchronism between Mode F and entropy/vorticity waves, the path of integration is deformed around the branch cut associated with this synchronism. This allows us to compute the inverse Fourier transform using only Mode F. The result is equal to that found by considering Mode F and the continuous spectrum together and integrating along the real α axis. Since the integrand associated with the sum of Mode F and the continuous spectrum is analytic, the choice of the integration path should not affect the result, and in fact, the numerical results for four choices of integration path agree very well.

For the 2D and 3D (fixed β) cases, the results for Mode S were compared with an asymptotic approximation of the Fourier integral. The first approximation used a Taylor series expansion of ω. Generally, this approximation compared favorably with the computed results. However, there is a significant discrepancy at the wave packet "tails." The asymptotic approximation was improved using numerically computed saddle point values. From a computational point of view, it is much faster to compute the wave packet using the asymptotic approximation with numerically computed saddle point values than it is to compute the inverse Fourier transform.

Additionally, the full 3D inverse Fourier transform was found for Mode S. Since the 3D spectrum is so complex, rather than compute the inverse Fourier transform, we have used an asymptotic approximation of the Fourier integral, with numerically computed saddle point values. A key feature of the 3D wave packet is its 2D nature. As discussed in Ref. 15, Mode S is a single discrete mode that corresponds to a single pole in the complex p plane. This single mode is comprised of Mack's first and second modes, and for this set of parameters, the most unstable section of Mode S is associated with Mack's second mode, whose maximum growth rate is associated with 2D disturbances. Thus, it is not surprising that for sufficiently large time, the 3D wave packet will have a 2D appearance. One should note that a comparison of Fig. 9(a) and Fig. 14(a) shows that the spanwise wave number has little effect on the growth rate. This is a hint of the two-dimensionality of the 3D wave packet.

The previous analysis has been performed under a parallel flow assumption. However, this analysis may be extended to the case of weakly non-parallel flows through the use of multiple scales methods. Discussion of this extension may be found in Ref. 15. For strongly nonparallel flows, one should consider a BiGlobal stability problem formulation.[30] Unlike the present analysis, the BiGlobal stability problem deals with a 2D PDE based generalized eigenvalue problem. However, it should be noted that the biorthogonal eigenfunction system formulation can be used in the analysis of BiGlobal instability problems (e.g. separated flow), and that we believe this is a worthwhile area of exploration.

ACKNOWLEDGMENTS

The authors would like to thank the National Science Foundation for providing a VIGRE graduate student fellowship to one of the authors. Additionally, this work was supported by the U.S. Air Force Office of Scientific Research. The authors benefitted from the valuable comments and suggestions of anonymous reviewers.

[1] A. D. Kosinov, A. A. Maslov, and S. G. Shevelkov, "Experiments on the stability of supersonic laminar boundary layers," J. Fluid Mech. **219**, 621 (1990).
[2] D. W. Ladoon and S. P. Schneider, "Measurements of controlled wave packets at Mach 4 on a cone at angle of attack," AIAA Paper 1998-0436, 1998.
[3] J. D. Schmisseur and S. P. Schneider, "Receptivity of the Mach-4 boundary-layer on an elliptic cone to laser-generated localized free-stream perturbations," AIAA Paper 1998-0532, 1998.
[4] A. A. Maslov, A. N. Shiplyuk, A. A. Sidorenko, and D. Arnal, "Leading-edge receptivity of a hypersonic boundary layer on a flat plate," J. Fluid Mech. **426**, 73 (2001).
[5] X. Zhong and Y. Ma, "Receptivity and linear stability of Stetson's Mach 8 blunt cone stability experiments," AIAA Paper 2002-2849, 2002.
[6] Y. Ma and X. Zhong, "Receptivity of a supersonic boundary layer over a flat plate. Part 1. Wave structures and interactions," J. Fluid Mech. **488**, 31 (2003).
[7] Y. Ma and X. Zhong, "Receptivity of a supersonic boundary layer over a flat plate. Part 2. Receptivity to free-stream sound," J. Fluid Mech. **488**, 79 (2003).
[8] I. V. Egorov, A. V. Fedorov, and A. V. Nechaev, "Receptivity of supersonic boundary layer on a blunt plate to acoustic disturbances," AIAA Paper 2004-0294, 2004.
[9] Y. Ma and X. Zhong, "Receptivity of a supersonic boundary layer over a flat plate. Part 3. Effects of different types of free-stream disturbances," J. Fluid Mech. **532**, 63 (2005).
[10] I. V. Egorov, A. V. Fedorov, and V. G. Soudakov, "Direct numerical simulation of supersonic boundary layer receptivity to acoustic disturbances," AIAA Paper 2005-0097, 2005.
[11] X. Wang and X. Zhong, "Receptivity of a Mach 8.0 flow over a sharp wedge with half-angle 5.3° to wall blowing-suction," AIAA Paper 2005-5025, 2005.
[12] P. Huerre and M. Rossi, "Hydrodynamic instabilities in open flows," in *Hydrodynamics and Nonlinear Instabilities*, edited by C. Godreche and P. Manneville (Cambridge University Press, New York, 1998), pp. 81–294.
[13] L. H. Gustavsson, "Initial-value problem for boundary layer flows," Phys. Fluids **22**, 1602 (1979).
[14] A. V. Fedorov and A. M. Tumin, "Initial-value problem for hypersonic boundary-layer flows," AIAA J. **41**, 379 (2003).
[15] E. Forgoston and A. M. Tumin, "Initial-value problem for three-dimensional disturbances in a compressible boundary layer," Phys. Fluids **17**, 084106 (2005).

[16]L. M. Mack, "Boundary-layer stability theory," JPL 900-277 (Jet Propulsion Laboratory, Pasadena, CA 1969).
[17]L. M. Mack, "Special course on stability and transition of laminar flow," AGARD Report 709, 1984.
[18]A. V. Fedorov, "Receptivity of a high-speed boundary layer to acoustic disturbances," J. Fluid Mech. **491**, 101 (2003).
[19]A. M. Tumin, "Biorthogonal eigenfunction system in the triple-deck limit," Stud. Appl. Math. **117**, 165 (2006).
[20]A. M. Tumin, "Three-dimensional spatial normal modes in compressible boundary layers," AIAA Paper 2006-1109, 2006.
[21]A. V. Fedorov and A. P. Khokhlov, "Prehistory of instability in a hypersonic boundary layer," Theor. Comput. Fluid Dyn. **14**, 359 (2001).
[22]J. D. Anderson, Jr., *Hypersonic and High Temperature Gas Dynamics* (AIAA, Reston, VA, 1989).
[23]S. P. Schneider, "Fabrication and testing of the Purdue Mach-6 quiet-flow Ludwieg tube," AIAA Paper 2000-0295, 2000.
[24]M. Gaster, "Propagation of linear wave packets in laminar boundary layers," AIAA J. **19**, 419 (1981).
[25]M. Gaster, "The development of a two-dimensional wavepacket in a growing boundary layer," Proc. R. Soc. London **384**, 317 (1982).
[26]M. Gaster, "The development of three-dimensional wave packets in a boundary layer," J. Fluid Mech. **32**, 173 (1968).
[27]N. Bleistein and R. A. Handelsman, *Asymptotic Expansions of Integrals* (Dover, New York, 1986).
[28]R. Wong, *Asymptotic Approximations of Integrals* (Society for Industrial and Applied Mathematics, Philadelphia, 2001).
[29]E. Forgoston, M. Viergutz, and A. Tumin, "Numerical and asymptotical study of three-dimensional wave packets in a compressible boundary layer," AIAA Paper 2006-3223, 2006.
[30]V. Theofilis, "Advances in global linear instability analysis of nonparallel and three-dimensional flows," Prog. Aerosp. Sci. **39**, 249 (2003).